Interacting bosons in a triple well: Preface of many-body quantum chaos

Karin Wittmann W., E. R. Castro, Angela Foerster, and Lea F. Santos

Interacting bosons in a triple well: Preface of many-body quantum chaos

Karin Wittmann W.,[1] E. R. Castro,[1] Angela Foerster,[1] and Lea F. Santos[2]

[1]*Instituto de Física da UFRGS, Porto Alegre, RS, Brazil*
[2]*Department of Physics, Yeshiva University, New York, New York 10016, USA*

Systems of interacting bosons in triple-well potentials are of significant theoretical and experimental interest. They are explored in contexts that range from quantum phase transitions and quantum dynamics to semiclassical analysis. Here, we systematically investigate the onset of quantum chaos in a triple-well model that moves away from integrability as its potential gets tilted. Even in its deepest chaotic regime, the system presents features reminiscent of integrability. Our studies are based on level spacing distribution and spectral form factor, structure of the eigenstates, and diagonal and off-diagonal elements of observables in relationship to the eigenstate thermalization hypothesis. With only three sites, the system's eigenstates are at the brink of becoming fully chaotic, so they do not yet exhibit Gaussian distributions, which resonates with the results for the observables.

I. INTRODUCTION

The interest in many-body quantum chaos has grown significantly in recent years due to its close connection with thermalization [1–3], scrambling of quantum information [4], and the fact that many-body quantum systems can now be studied experimentally in a controllable way with a variety of experimental set-ups, from cold atoms and ion traps to superconducting devices and nuclear magnetic resonance. In studies of many-body quantum chaos, the focus is usually on interacting lattice systems with many sites and many particles, where the Hilbert space grows exponentially with the system size. Here, instead, we investigate the onset of quantum chaos in a system that has only three wells, but where the number N of particles is large. The Hilbert space grows quadratically with N, and as N increases, the system is brought closer to the classical limit.

Fascinating phenomena are explored with systems of interacting atoms in triple-well potentials, such as transistor-like behaviors [5–7], entanglement generation [8, 9], coherent population transfer [10–13], fragmentation [14, 15], quantum-classical correspondence [16–22], quantum chaos [23–30], superfluidity [31, 32], localization [33], and caustics [34], among others [35–47]. One of the most popular models in this context is the three-well Bose-Hubbard model with short-range interactions and local hopping terms [48, 49]. This system, with three or more wells, is in general not integrable [19, 21, 27, 30, 50–53]. Integrability is achieved with two or with an infinite number of wells.

A bosonic triple-well model with an integrable limit was introduced in Ref. [54] and explored for switching devices [55],[56]. This model is a member of a family of quantum integrable multi-well tunneling systems that have the two-site Bose-Hubbard model [57–59] as a leading constituent. Integrability requires the presence of long-range couplings, which is in fact a physical condition for ultracold dipolar bosons with large dipole moment, such as chromium, erbium, or dysprosium. Dipolar cold atoms provide a rich platform for the study of mesoscopic quantum superpositions [37], macroscopic cat states [60],

quantum droplets [61], and supersolid states [62].

By tilting the potential [55], the bosonic triple-well model introduced in [54] becomes chaotic. We provide a systematic study of this transition based not only on spectral correlations, but also on the structure of the eigenstates and its consequences to the eigenstate expectation values and the distributions of the off-diagonal elements of the number operator of each well, in close connection with the notion of the eigenstate thermalization hypothesis (ETH).

Contrary to systems where the number of wells and particles are increased, the number of degrees of freedom in the triple-well model is fixed. Increasing its number of bosons does not enhance its chaotic features. The range of values of the integrability breaking parameter that leads to chaos is not extended for larger N's and the eigenstates do not reach higher degrees of ergodicity. Even for energies close to the middle of the spectrum, for which a semiclassical analysis gives positive Lyapunov exponents [63], the distributions of the components of the eigenstates and of the off-diagonal elements of the number operators are not Gaussian, which contrasts with what happens for multi-well systems.

In non-driven systems, three wells constitute the turning point for the onset of many-body quantum chaos. The transition from integrability to chaos does take place, but with some reminiscence of integrability.

The paper is organized as follows. The model is described in Sec. II. The analysis of the spectrum and level repulsion are presented in Sec. III. The core of the work is the detailed study of the structure of the eigenstates in Sec. IV and its consequence to the diagonal and off-diagonal elements of the number operators in Sec. V. Conclusions are given in Sec. VI.

II. MODEL

The quantum system that we study consists of N bosons in an aligned triple-well potential described by the following Hamiltonian [55],

$$\hat{H} = \frac{U}{N} \left(\hat{N}_1^2 + \hat{N}_2^2 + \hat{N}_3^2 \right) + \epsilon \left(\hat{N}_3 - \hat{N}_1 \right)$$
$$+ \frac{2U}{N} \left(-\hat{N}_1 \hat{N}_2 - \hat{N}_2 \hat{N}_3 + \hat{N}_1 \hat{N}_3 \right)$$
$$+ \frac{J}{\sqrt{2}} \left(\hat{a}_1^\dagger \hat{a}_2 + \hat{a}_2^\dagger \hat{a}_1 \right) + \frac{J}{\sqrt{2}} \left(\hat{a}_2^\dagger \hat{a}_3 + \hat{a}_3^\dagger \hat{a}_2 \right), \quad (1)$$

where $\hat{N}_i = \hat{a}_i^\dagger \hat{a}_i$ is the number operator of the well i, $\hat{a}_i$ ($\hat{a}_i^\dagger$) is the annihilation (creation) operator, U is the onsite interaction strength and also the strength of the interactions between wells, J is the tunneling amplitude between wells, and ϵ is the amplitude of the tilt between the wells. We consider repulsive interaction, $U \geq 0$.

Hamiltonian (1) conserves the total number of bosons, $N = N_1 + N_2 + N_3$, and when $\epsilon = 0$, it commutes with the parity operator. The matrix has dimension $D = (N + 2)!/(2!N!)$. Our studies of the structure of the eigenstates are done in the Fock basis, $|n\rangle = |N_1, N_2, N_3\rangle$. We denote the eigenstates and eigenvalues of $\hat{H}$ by $|\alpha\rangle$ and E_α.

A schematic representation of our model is shown in Fig. 1. When $\epsilon = 0$ [Fig. 1 (a)], the model is integrable and solvable with the algebraic Bethe ansatz [54]. At this point, in addition to energy and the total number of particles, our three-degree-of-freedom model has a third independent conserved quantity, $Q = J^2 N_3/2 + J^2 N_1/2 - J^2(a_1^\dagger a_3 + a_3^\dagger a_1)/2$ [54, 55]. The system becomes nonintegrable [Fig. 1 (b)] when the tilt is included. As discussed in Sec. III A, the model shows signatures of quantum chaos when the tilt amplitude is of the order of the hopping and interaction strengths, $\epsilon \sim J, U$.
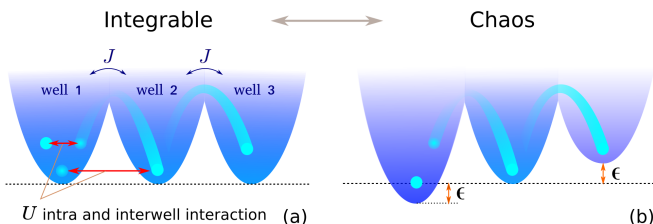

FIG. 1. Schematic representation of the three-well system described by Eq. (1) for both the integrable (a) and the nonintegrable (b) regime. The red arrows indicate the intrawell and interwell interaction strength U, the black arrows indicate the tunneling amplitude J between adjacent wells, and ϵ represents the tilt of the potentials of wells 1 and 3 with respect to well 2.

In the absence of the potential tilt and of the interaction between wells, our model coincides with the bare Bose-Hubbard model with 3 sites. Signatures of quantum chaos were studied in this model, for example, in [19, 30]. This case and also the extended triple-well Bose-Hubbard model with dipolar interaction [37] exhibit properties similar to those of our system in the chaotic domain. Comparisons between the three models are presented in the appendix A.

A. Parameters and density of states

In our numerical analysis, we fix $J = 1$, $U/J = 0.7$, and vary ϵ for different numbers of particles. The choice of U is justified with Fig. 2 (a), where we show the eigenvalues as a function of the interaction strength for $\epsilon = 0$. When $U = 0$, there is only hopping and the model is trivially solved. This is usually referred to as Rabi regime [55] in analogy with the double-well model [57, 64]. As the interaction strength increases and becomes larger than the hopping amplitude, $U/J > 1$, energy bands are formed. The extreme scenario of $U \gg J$ is the Fock regime, where the eigenstates approach the Fock states, and the model is again trivially solved. The region where we can expect chaos to develop is therefore for $0 < U/J < 1$, which explains the choice $U/J = 0.7$ indicated with the red dotted vertical line in Fig. 2 (a).
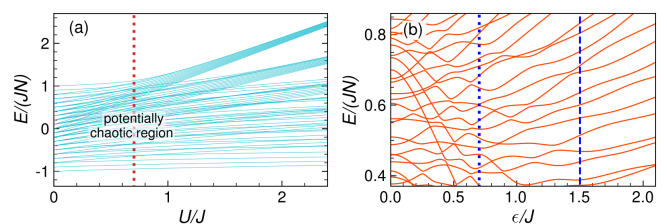

FIG. 2. Normalized eigenvalues as a function of the interaction strength, U/J, for $\epsilon = 0$ (a) and as a function of the tilt amplitude, ϵ/J, for $U/J = 0.7$ (b). The vertical line in Fig. 2 (a) marks the value $U/J = 0.7$, which is used in panel (b) and in all of our subsequent studies. In Fig. 2 (b), the vertical lines marks the values $\epsilon/J = 0.7$ (dotted line) and $\epsilon/J = 1.5$ (dashed line) used in our studies of the chaotic regime. In all panels N=10.

In chaotic systems, the eigenvalues are correlated and avoid each other [65, 66], while in integrable models (apart from the picket-fence scenario [67–69]), the energy levels can cross. This difference is clearly seen in Fig. 2 (b), where we fix $U/J = 0.7$ and vary ϵ/J. Level crossing happens when $0 \leq \epsilon/J < 1$, but is avoided for $\epsilon/J \gtrsim 1$, where the "spaghetti structure", typical of repulsive energy levels, becomes visible.

In Fig. 3, we compare the density of states (DOS),

$$\nu(E) = \sum_{\alpha=1}^{D} \delta(E - E_\alpha), \quad (2)$$

of the model (1) for three values of the tilt, $\epsilon/J = 0$, 0.7, and 1.5. In realistic interacting many-body quantum systems with many degrees of freedom, such as spin models with many excitations [70] or Bose-Hubbard models with many particles and many sites [51, 71], the DOS is typically Gaussian [72, 73], which can be explained using the central limit theorem. This contrasts with our model [Figs. 3 (a)-(c)], which has few degrees of freedom.

Systems with few-degrees of freedom, such as the Dicke model [74], spin-1/2 models with less than 4 excitations [75], and multi-well Kronig-Penney-like systems

with few particles [76], often present shapes other than Gaussian. We see in the appendix A that the bare triple-well Bose-Hubbard model and the extended triple-well Bose-Hubbard model show distributions that, similarly to our model in Fig. 3 (c), are not yet Gaussian, but get close to it. The DOS for the extended Bose-Hubbard model and for our model are comparable, since both have long-range couplings.
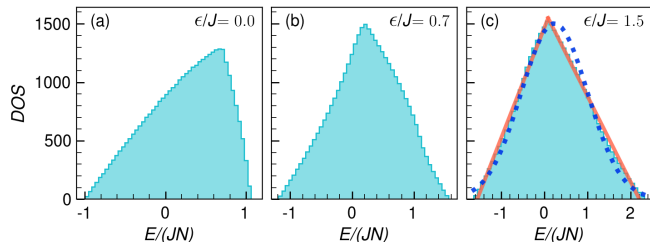

FIG. 3. Density of states for $N = 270$, $U/J = 0.7$, and $\epsilon/J = 0$ (a), 0.7 (b) and 1.5 (c). The solid line in (c) is a linear fitting for the left and right sides of the distribution, while the dotted line is a Gaussian distribution fitting.

III. SPECTRAL CORRELATIONS

To quantify the degree of correlations between the eigenvalues, we study the level spacing distribution and the spectral form factor. We show that for $U/J \sim 0.7$, as ϵ in Eq. (1) increases from zero, our triple-well model leaves the integrable point ($\epsilon = 0$) and moves towards the chaotic domain.

A. Level spacing distribution

The transition to quantum chaos can be verified with the distribution $P(s)$ of the spacings s between nearest unfolded energy levels. For chaotic systems with real and symmetric Hamiltonian matrices, as in Eq. (1), $P(s)$ follows the Wigner surmise [66, 77], $P_W(s) = (\pi s/2) \exp\left(-\pi s^2/4\right)$, as obtained also for the eigenvalues of full random matrices from a Gaussian orthogonal ensemble (GOE). This distribution indicates that the eigenvalues are correlated and repel each other, that is, $P(s = 0) = 0$. In integrable models, the level spacing distribution is Poissonian, $P_P(s) = e^{-s}$, since the energy levels are uncorrelated [78].

The analysis of the level spacing distribution requires unfolding the eigenvalues and separating them by symmetry sectors. The unfolding procedure corresponds to rescaling the eigenvalues, so that the local density of states of the rescaled energies is 1. The separation by subspaces is necessary, because eigenvalues from different symmetry sectors have no reason to be correlated.

In Figs. 4 (a)-(c), we illustrate $P(s)$ for $\epsilon/J = 0$, 0.7, and 1.5, respectively. The Poissonian distribution is ob-

tained for the integrable point $\epsilon = 0$ in Fig. 4 (a), and the Wigner shape is seen for $\epsilon/J = 1.5$ in Fig. 4 (c), as we had anticipated from the "spaghetti structure" in Fig. 2 (b). An intermediate picture emerges for $\epsilon/J = 0.7$ in Fig. 4 (b).
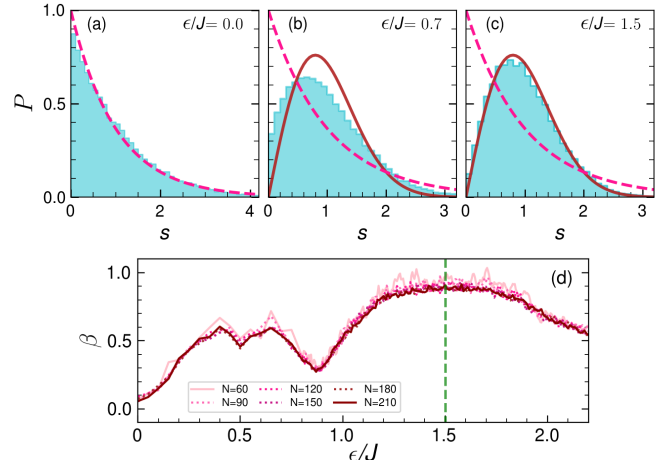

FIG. 4. Level spacing distribution for $N = 270$ and $\epsilon/J = 0$ (a), $\epsilon/J = 0.7$ (b), and $\epsilon/J = 1.5$ (c); and chaos indicator β as a function of the tilt amplitude for various N's (d). In (a)-(c): The dashed (solid) line represents the Poissonian (Wigner) distribution. In (d): The green vertical line at $\epsilon/J = 1.5$ marks where β gets the closest to 1, indicating the Wigner distribution.

The proximity of the level spacing distribution to the Poissonian or the Wigner distribution can be quantified with the chaos indicator β, which is obtained by fitting $P(s)$ with the Brody distribution [73] (see also [79]),

$$P_\beta(s) = (\beta+1)bs^\beta \exp(-bs^{\beta+1}), \quad b = \left[\Gamma\left(\frac{\beta+2}{\beta+1}\right)\right]^{\beta+1}$$
(3)

For chaotic systems, $\beta \sim 1$ and for a Poissonian distribution, $\beta \sim 0$.

In Fig. 4 (d), we show β as a function of ϵ/J for $N = 60, 90, \ldots, 210$. As evident from the figure, a high degree of chaos happens for $\epsilon/J \in [1.3, 1.7]$. Notice that this range of values does not grow as N increases, which contrasts with interacting many-body quantum systems with many sites [80–82], where studies of chaos indicators for different system sizes suggest that in the thermodynamic limit, an infinitesimal integrability breaking term may be enough to bring those systems to the chaotic domain. In addition and also contrary to the results for systems with many sites [81, 82], larger values of N do not take β closer to 1. The only effect that an increased value of N appears to have for the triple-well model is to reduce the fluctuations in the values of β for nearby ϵ's, which concurs with improved statistics.

B. Spectral form factor

The level spacing distribution detects only short-range correlations. To get a better idea of the degree of spectral correlations, one may resort to other indicators of quantum chaos, such as the spectral form factor,

$$S_{FF}(t) = \left\langle \left| \sum_{\alpha=1}^{D} f(E_\alpha)e^{-iE_\alpha t} \right|^2 \right\rangle, \quad (4)$$

which captures both short- and long-range correlations. The spectral form factor is used to study level statistics in the time domain. When the eigenvalues are correlated as in random matrices, $S_{FF}(t)$ develops the so-called correlation hole [83–88], which we further discuss below Eq. (11). The spectral form factor is advantageous over the direct analysis of the eigenvalues, because it does not require unfolding the spectrum or separating the eigenvalues by symmetry sectors [82, 89], although averages, indicated by $\langle . \rangle$ in Eq. (4), are needed, since this quantity is non-self-averaging [90, 91].

A filter function $f(E_\alpha)$, as used in Eq. (4), is often added to the spectral form factor [92]. When $f(E_\alpha)$ coincides with the components of an initial state projected in the energy eigenbasis, the spectral form factor becomes the survival probability [91]. In our analysis, we choose [93]

$$f(E_\alpha) = \frac{r_\alpha g(E_\alpha)}{\sum_\beta r_\beta g(E_\beta)}, \quad (5)$$

where r_α are random numbers from a uniform distribution in the interval $[0, 1]$, the function $g(E) = \rho(E)/\nu(E)$, and $\rho(E)$ is a chosen energy profile, which, in our case, is a rectangular function,

$$\rho(E) = \begin{cases} \dfrac{1}{2\sigma} & \text{for } E \in [E_c - \sigma, E_c + \sigma] \\ \\ 0 & \text{otherwise,} \end{cases} \quad (6)$$

of width σ, centered at the energy E_c, and with bounds at $E_{min} = E_c - \sigma$ and $E_{max} = E_c + \sigma$. The division of $\rho(E)$ by $\nu(E)$ is done using the linear fits for the DOS in Fig. 3 (c). This procedure compensates for variations in the density of states and ensures the rectangular shape of the filter function [93]. As it will become clear in Sec. IV, the region where the eigenstates are mostly chaotic happens for $E/(JN) \in [-0.2, 1]$. For this reason, we choose $E_c/(JN) = 0.5$ and $\sigma/(JN) = 0.35$.

In Fig. 5, we consider a large Hilbert space and show $S_{FF}(t)$ in the chaotic region of strong level repulsion averaged over various realizations of the random numbers r_α and taking into account also a moving time average starting at $t \sim 5/J$, where the fluctuations are large. The numerical results are presented together with the analytical expression obtained following Refs. [93–95],

$$S_{FF}^{analyt}(t) = \frac{1 - \langle \overline{S_{FF}} \rangle}{\eta - 1} \left[\eta \frac{\sin^2(\sigma t)}{(\sigma t)^2} - b_2 \left(\frac{t}{2\pi\nu_c} \right) \right] + \langle \overline{S_{FF}} \rangle, \quad (7)$$

where

$$\eta = \frac{\langle r_\alpha^2 \rangle}{\langle r_\alpha \rangle^2 \langle \overline{S_{FF}} \rangle} = \frac{4}{3\langle \overline{S_{FF}} \rangle}$$

is the effective dimension associated with the chosen filter function, and

$$\nu_c = \frac{\eta}{2\sigma} \quad (8)$$

is the density of states at $E = E_c$, or equivalently, the inverse mean level spacing probed by the chosen energy profile [93].
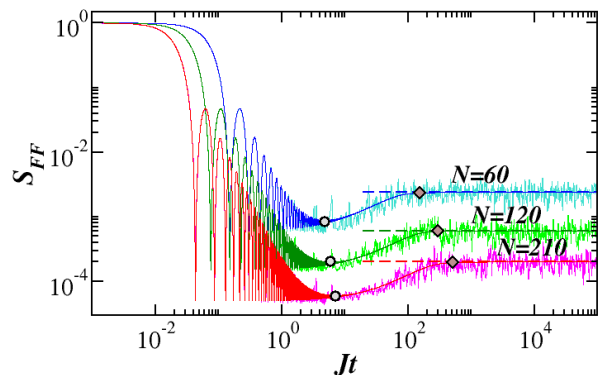

FIG. 5. Spectral form factor for three values of N. The lines with fluctuations, which have lighter colors, represent numerical results; the thin smooth lines give the analytical expression in Eq. (7); and the dashed horizontal lines indicate the saturation point $\langle \overline{S_{FF}} \rangle$ in Eq. (11). The symbols mark the time to reach the minimum of the correlation (circle) and the saturation time (diamond). For the numerical results: Averages over 500 random realizations and also running averages.

The first term in the square brackets of Eq. (7) describes the behavior of $S_{FF}(t)$ at short times. It is obtained by writing Eq. (4) as an integral,

$$S_{FF}(t) = \left\langle \left| \int_{E_{min}}^{E_{max}} \rho_0(E)e^{-iEt}dE \right|^2 \right\rangle, \quad (9)$$

and substituting the energy distribution,

$$\rho_0(E) = \sum_{\alpha=1}^{D} f(E_\alpha)\delta(E - E_\alpha), \quad (10)$$

with the smoothed energy profile $\rho(E)$ from Eq. (6), which can be done for large Hilbert spaces. The Fourier transform in Eq. (9) gives $\dfrac{\sin^2(\sigma t)}{(\sigma t)^2}$. This function leads to a power-law decay with exponent 2 due to the bounds of the filter function [96–98].

The effects of the spectral correlations get manifested at larger times, when the discreteness of the spectrum is resolved and the correlations are then detected. This

results in the dip in Fig. 5 below the horizontal dashed line that represents the infinite-time average

$$\langle \overline{S_{FF}} \rangle = \sum_\alpha |f(E_\alpha)|^2. \tag{11}$$

This dip is known as correlation hole [83–88] and it does not exist in models that present a Poissonian level spacing distribution. In the case of GOE full random matrices, the dip is described by the two-level form factor [77],

$$b_2(\bar{t}) = \begin{cases} 1 - 2\bar{t} + \bar{t}\ln(2\bar{t} + 1) & \bar{t} \leq 1 \\ \bar{t}\ln\left(\dfrac{2\bar{t} + 1}{2\bar{t} - 1}\right) - 1 & \bar{t} > 1 \end{cases}. \tag{12}$$

This function describes very well our numerical results and confirms the chaoticity of our triple-well model.

By comparing the results for different numbers of bosons in Fig. 5, it is clear that the time to reach the minimum of the correlation hole and the time to reach saturation increase with N. Analytical expressions for these times are given in the appendix B 1. They are much shorter than those obtained for interacting many-body quantum systems with many sites [95].

IV. EIGENSTATES

In chaotic quantum systems, the eigenvalues are correlated and the eigenstates are uncorrelated. In this section, we analyze the transition to quantum chaos through the changes in the structure of the eigenstates. As ϵ increases from zero and the system moves from the integrable to the chaotic domain, we expect the eigenstates away from the edges of the spectrum to become closer to the eigenstates of GOE full random matrices [1, 2]. The GOE eigenstates are random vectors with components that are real and which correspond to independent Gaussian random numbers satisfying the normalization condition. In realistic many-body quantum systems, a fraction of the components of the chaotic eigenstates can be nearly zero, but the nonzero components follow a Gaussian distribution [70].

To detect the onset of chaotic eigenstates, one can employ measures of delocalization [79, 99] and fractality [71], and analyze the distributions of the components of the eigenstates. These methods are, of course, attached to a basis choice. We use here the Fock basis, $|n\rangle$, which are the eigenstates of the number operators studied in Sec. V. This basis is in close connection with cold-atom experiments, where dynamics are initiated by preparing the system in Fock states. Nevertheless, in the appendix B 3 and appendix B 4, we also provide the analysis of the eigenstates using as basis the eigenstates of the $\hat{H}(\epsilon = 0)$ part of the total Hamiltonian in Eq. (1). Our main conclusion that the components of the eigenstates of the triple-well model do not follow a Gaussian distribution holds for either choice of basis.

Even the most delocalized eigenstates of our triple-well model are not fully chaotic. A similar conclusion can be drawn for the triple-well Bose-Hubbard model in Ref. [30]. The anomalous scaling of the eigenstate-to-eigenstate fluctuations of expectation values of local observables with the Hilbert space found in that work might be attributed to eigenstates that are not fully chaotic.

A. Delocalization Measures

In Figs. 6 (a)-(c), we show the Shannon entropy, S_h^α, of each eigenstate $|\alpha\rangle$ written in the Fock basis $|n\rangle$,

$$S_h^\alpha \equiv -\sum_{n=1}^D |C_n^\alpha|^2 \ln |C_n^\alpha|^2, \tag{13}$$

as a function of energy. In the equation above, $C_n^\alpha = \langle n|\alpha\rangle$. This entropy measures the degree of delocalization of the eigenstates in the chosen basis. If the eigenstate coincides with a basis vector, there is a single $|C_n^\alpha|^2 = 1$ and the state is completely localized. In this case, $S_h^\alpha = 0$. If the eigenstate is homogeneously spread in the Hilbert space, being therefore completely delocalized, then all $|C_n^\alpha|^2 = 1/D$ and the entropy reaches its maximum value $S_h^\alpha = \ln(D)$. An equivalent measure of delocalization is the participation ratio,

$$P_R^\alpha \equiv \sum_{n=1}^D \frac{1}{|C_n^\alpha|^4}, \tag{14}$$

whose figures are provided in the appendix B 2. The participation ratio was also considered in the analysis of the triple-well Bose-Hubbard model in Ref. [30].

For GOE full random matrices, the components C_n^α of the eigenstates are independent real random variables from a Gaussian distribution with weights $|C_n^\alpha|^2$ that fluctuate around $1/D$, so $S_h^{\text{GOE}} \sim \ln(0.48D)$. In Figs. 6 (a)-(c), we show S_h^α divided by S_h^{GOE}.

In the integrable regime [Fig. 6 (a)], we see a pattern of lines that must be associated with periodic orbits, likely to be found in the phase space of the classical limit of our model. This subject will be discussed in detail in a future publication [100]. As ϵ/J increases, regions of chaos begin to emerge [Fig. 6 (b)], where the fluctuations decrease significantly and S_h^α reaches values closer to S_h^{GOE}, as in the vicinity of $E/(JN) \sim 0.3$ and $E/(JN) \sim 0.9$. For $\epsilon/J = 1.5$ [Fig. 6 (c)], an evident chaotic region emerges for $E/(JN)$ in the interval given approximately by [-0.2,1]. This energy range explains our choice for $E_c/(JN) = 0.5$ in the analysis of the spectral form factor in Eq. (6). We have also verified that the semiclassical analysis of the model in this region of energy leads to positive Lyapunov exponents [63].

Notice, however, that the regular pattern of lines seen in Fig. 6 (a) persists in the edges of the spectrum for Fig. 6 (b) and even for Fig. 6 (c). Our system is clearly
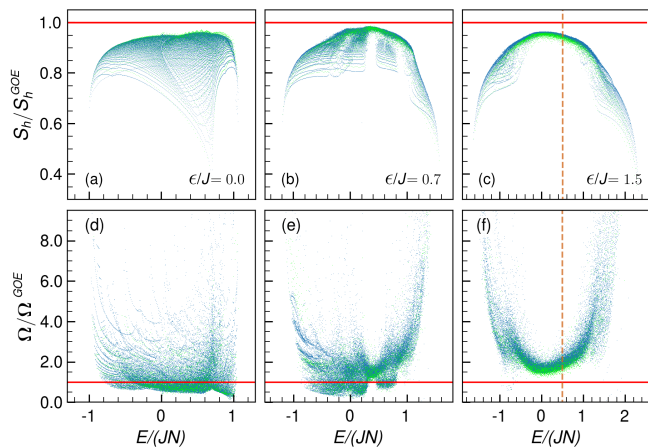
FIG. 6. Shannon entropy S_h and overlaps of neighboring eigenstates Ω as a function of energy for $N = 90$ (light lime dots) and $N = 270$ (dark blue dots). In (a) and (d): $\epsilon/J = 0$, in (b) and (e): $\epsilon/J = 0.7$, and in (c) and (f): $\epsilon/J = 1.5$. The solid horizontal lines mark the results for GOE full random matrices. The dashed vertical lines in (c) and (f) mark approximately the center of the chaotic region.

separated into regions of chaos and non-chaos, independently of the number of bosons. This is confirmed by comparing the results for $N = 90$ (light color) and $N = 270$ (dark color) in Fig. 6 (c).

In Figs. 6 (d)-(f), we show the quantity $\Omega_{\alpha,\alpha'}$ first proposed in Ref. [70] to measure how similar two neighboring eigenstates $|\alpha\rangle$ and $|\alpha'\rangle$ are,

$$\Omega_{\alpha,\alpha'} \equiv \sum_{n=1}^{D} |C_n^{\alpha}|^2 |C_n^{\alpha'}|^2. \tag{15}$$

In full random matrices, where the components $|C_n^{\alpha}|^2$ and $|C_n^{\alpha'}|^2$ are uncorrelated Gaussian random numbers, $\Omega^{\text{GOE}} \sim 1/D$. Correlations result in values of $\Omega_{\alpha,\alpha'} > 1/D$. Large values of $\Omega_{\alpha,\alpha'}$ and large fluctuations are found throughout the spectrum of the integrable model [Fig. 6 (d)], while in the chaotic domain [Fig. 6 (f)] they are restricted to the edges of the spectrum, $E/(JN) < -0.2$ and $E/(JN) > 1$, where chaos does not develop. Notice, however, that even in the chaotic region, $\Omega > \Omega^{\text{GOE}}$, which indicates that some level of correlation among the components persists.

To get some insight on how the level of correlations depend on N, in Figs. 7 (a)-(c), we select the eigenstates in the chaotic region with energies $E/(JN) \in [0.4, 0.6]$ and study how the averages over these states for $\langle S_h \rangle / S_h^{GOE}$, $\langle \Omega \rangle / \Omega^{GOE}$, and $\langle P_R \rangle / P_R^{GOE}$ change from $N = 60$ to $N = 270$. The analysis is done with box-and-whisker plots [101], which displays the data distribution through its quartiles. The horizontal line drawn in the middle of the boxes indicates the median and the whiskers (the lines extending from the boxes) indicate variability outside the upper and the lower quartiles. The averages are marked with symbols.
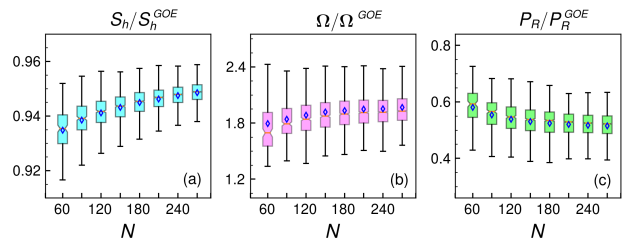

FIG. 7. Box-and-whisker plots for the Shannon entropy (a), overlaps of neighboring eigenstates (b), and participation ratio (c) for various N's. The data range comprises eigenstates with energies $E/(JN) \in [0.4, 0.6]$ from those presented in Fig. 6 (c), where $U/J = 0.7$ and $\epsilon/J = 1.5$. The median for each N is marked with the orange line inside each box and the average with the diamond symbol.

The medians in Fig. 7 change as N grows. The fact that the values for all three quantities are below those for random matrices is understandable, since we are dealing with the eigenstates of realistic systems with two-body couplings, so some level of correlation always exists. It calls attention, however, that the normalized averages for the entropy grows with N [Fig. 7 (a)], while the averages for Ω [Fig. 7 (b)] and P_R [Fig. 7 (c)] move further away from the random matrix results. The overlaps of neighboring states and the participation ratio are more sensitive to fluctuations in the tails of their distributions than the Shannon entropy, due to the logarithm present in the latter [102].

We note that the growth of $\langle \Omega \rangle / \Omega^{\text{GOE}}$ and the decay of $\langle P_R \rangle / P_R^{\text{GOE}}$ with N in Fig. 7 are not artifacts of the Fock basis. They hold also for the basis corresponding to the eigenstates of $\hat{H}(\epsilon = 0)$ [not shown].

From Fig. 7 (c), it is not possible to conclude whether $\langle P_R \rangle / P_R^{\text{GOE}}$ tends to a constant for larger N's or keeps decreasing. The latter would imply absence of fully developed chaos, in contrast with what is observed for chaotic multi-well systems, and would suggest multifractality. Motivated by this discussion, the next subsection investigates whether the eigenstates with energies in the most chaotic region, those with $E/(JN) \sim 0.5$, might indeed be multifractal.

B. Multifractality

For a state that is extended, but not fully delocalized, $\langle P_R \rangle$ is not proportional to P_R^{GOE}. This can be indicated by writing $\langle P_R \rangle \propto D^{-D_2}$, where D_2 is known as the generalized dimension. If $D_2 = 1$, the state is fully delocalized and $\langle P_R \rangle \propto P_R^{\text{GOE}}$. When $D_2 = 0$, the state is localized in the chosen basis. Contrary to these two cases, for $0 < D_2 < 1$, the state is fractal, meaning that it is extended, but not ergodic.

The analysis of multifractality requires one further step. To verify whether a state is multifractal, we study how the generalized dimension D_q, obtained from the

generalized inverse participation ratio, $I_{PR}^q = \sum_n |C_n^\alpha|^{2q}$, depends on q [103, 104]. The generalized dimension is extracted from the scaling analysis of

$$\langle I_{PR}^q \rangle \propto D^{-(q-1)D_q}. \tag{16}$$

Multifractality implies that $0 < D_q < 1$ and that D_q exhibits a nonlinear behavior with q.

We extract the generalized dimension D_q for the eigenstates with energy $E/(JN) \sim 0.5$ by analyzing how $\langle I_{PR}^q \rangle$ scales with the Hilbert space dimension D. The slope of the curve for $\ln\langle I_{PR}^q \rangle$ as a function of $\ln D$ gives D_q, as illustrated in Fig. 8 (a) for $q = 0.5$ and Fig. 8 (b) for $q = 1.5$, where we vary the dimension of the Hilbert space from $D = 1\,891$ (for $N = 60$) to $D = 36\,856$ (for $N = 270$).
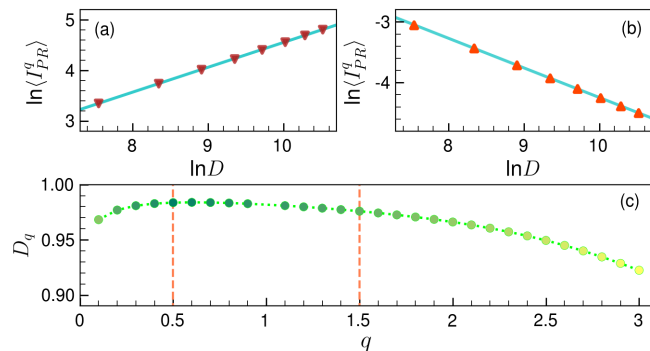

FIG. 8. Scaling analysis of the generalized inverse participation ratio averaged over 300 eigenstates with $E/(JN) \sim 0.5$ for $q = 0.5$ in (a) and $q = 1.5$ in (b), and generalized dimension D_q as a function of q in (c); $\epsilon/J = 1.5$. In (a) and (b), the solid line is a linear fitting and the symbols are the numerical results obtained by varying the dimension of the Hilbert space from $D = 1\,891$ ($N = 60$) to $D = 36\,856$ ($N = 270$).

Our results for D_q as a function of q are shown in Fig. 8 (c). The values of D_q are larger than 0.9, but always smaller than 1, and they are nonlinear in q, suggesting multifractality.

C. Distribution of Components

The discussion above prompts a more detailed analysis of the components of the eigenstates. We select a representative eigenstate $|\alpha\rangle = \sum_n C_n^\alpha |n\rangle$ with energy $E/(JN) \sim 0.5$. The distribution of its components in Fig. 9 (a) shows a high peak at $C_n^\alpha \sim 0$. This excessive number of zero amplitudes comes mostly from the Fock states that have energy $e_n = \langle n|H|n\rangle$ outside the chaotic region, that is $e_n/J < -0.2$ or $e_n/J > 1$. By removing the components associated with these states, the peak is erased, as seen in Fig. 9 (b). The remaining Fock states constitute 59% of the Hilbert space, but they are the main constituents of the selected eigenstate, leading to

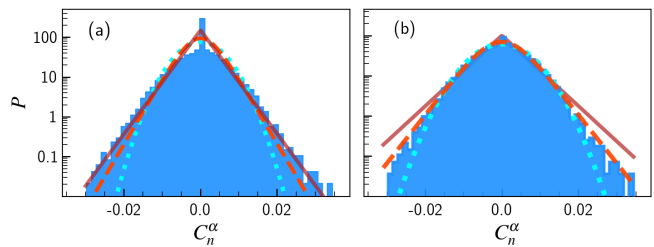$$\sum_{\substack{n \\ -0.2 \le e_n/J \le 1}} |C_n^\alpha|^2 = 0.90.$$

FIG. 9. Distribution of the components C_n^α of an eigenstate with energy $E/(JN) \sim 0.5$; $\epsilon/J = 1.5$, $N = 270$. In (a), all components are considered, while in (b), only those for which $-0.2 \le e_n/J \le 1$. Solid line: Laplace distribution; dashed line: Logistic distribution; dotted line: Gaussian distribution.

The best distribution in Fig. 9 (a) is Laplace. After removing the peak, in Fig. 9 (b), the best distribution becomes Logistic, which is more similar to a Gaussian, but exhibits longer tails. A Gaussian distribution is what one would expect for a fully chaotic state. This is the distribution obtained for the components of the eigenstates of full random matrices and also for chaotic systems with many wells and particles. Thus, the analysis in Fig. 9 shows that the eigenstates of our triple-well model do not reach fully chaotic structures. A similar conclusion is reached when the zero-detuning basis is employed, as shown in the appendix B 4.

The lack of ergodicity of the eigenstates is valid also for the triple-well Bose-Hubbard models presented in the appendix A. The distributions of the components of their most delocalized eigenstates are also Logistic.

V. EIGENSTATE THERMALIZATION HYPOTHESIS

Chaotic eigenstates explain and ensure the validity of the eigenstate thermalization hypothesis (ETH) [80, 105]. The ETH says that when the eigenstate expectation values of a few-body observable $\mathcal{O}$, that is $\mathcal{O}_{\alpha\alpha} = \langle\alpha|\hat{\mathcal{O}}|\alpha\rangle$, are smooth functions of the eigenenergies, these values approach the result from the microcanonical ensemble, $\mathcal{O}_{mic}$, as the system size increases [3]. The hypothesis is also attached to the conditions of absence of degeneracies and $\mathcal{O}_{\alpha\beta} \ll \mathcal{O}_{\alpha\alpha}$, where $\mathcal{O}_{\alpha\beta} = \langle\beta|\hat{\mathcal{O}}|\alpha\rangle$ are the off-diagonal elements of the observable. These are the prerequisites for thermalization, where the infinite-time average of the observable coincides with its thermodynamic average.

In the case of interacting many-body quantum systems, the onset of chaotic eigenstates also leads to the Gaussian distribution of the off-diagonal elements of few-body observables [106], [107]. In this section, we investigate the consequences that the lack of gaussianity of the eigenstates of our model has on the diagonal and off-diagonal elements of the number operator of each well. This observable, which is diagonal in the Fock basis, is chosen for its experimental accessibility.

A. Diagonal Elements

We start the analysis by investigating the diagonal elements of $\hat{N}_i$ in Fig. 10. As the integrability breaking term increases from $\epsilon/J = 0$ in Fig. 10 (a) to $\epsilon/J = 1.5$ in Fig. 10 (c), the fluctuations decrease significantly, reflecting the similar behavior of the eigenstates illustrated in Fig. 6. For the integrable model in Fig. 10 (a), there is a clear regular structure, and $(N_1)_{\alpha\alpha} = (N_3)_{\alpha\alpha}$ due to the Hamiltonian parity symmetry. In Fig. 10 (b), smaller fluctuations appear for $E/(JN) \sim 0.3$ and $E/(JN) \sim 0.9$, as it happens also for the entropy in Fig. 6 (b). In Fig. 10 (c), smaller fluctuations are seen throughout the spectrum, consistent with the notion of ETH. Notice, however, that outside the chaotic region, for $E/(JN) < -0.2$ and $E/(JN) > 1$, one still sees regular structures that resemble the pattern of lines seen for the eigenstates in Fig. 6 (c).

Close to $E/(JN) \sim 0.5$ in Fig. 10 (c), the population inversion, where $(N_2)_{\alpha\alpha}$ (red) and $(N_3)_{\alpha\alpha}$ (green) become larger than $(N_1)_{\alpha\alpha}$ (blue), is consistent with the tilt, which causes states with occupation on site 2 and, especially, on site 3 to have larger energies than states with population on site 1. For very high energies, it is therefore natural that $(N_1)_{\alpha\alpha} \simeq (N_2)_{\alpha\alpha} \to 0$. In contrast, for low energies, the distribution of particles is relatively symmetric around $(N_2)_{\alpha\alpha}$, with $N_1 > N_2 > N_3$ and $(N_3)_{\alpha\alpha} \to 0$, as expected.
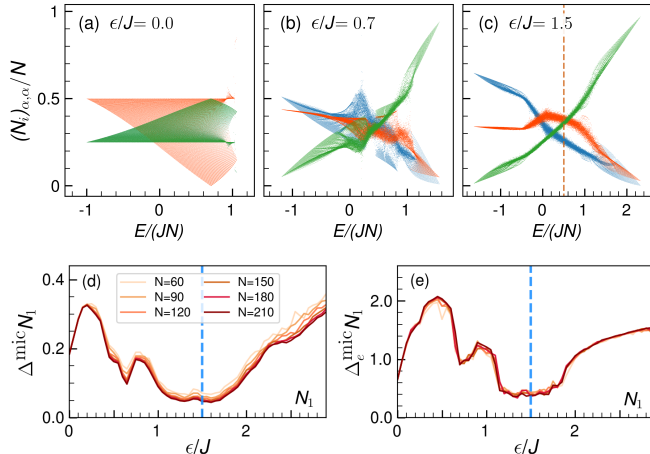

FIG. 10. Eigenstate expectation values for $(N_1)_{\alpha,\alpha}$ (blue), $(N_2)_{\alpha,\alpha}$ (red), and $(N_3)_{\alpha,\alpha}$ (green) as a function of energy, for $\epsilon/J = 0.0$ (a), $\epsilon/J = 0.7$ (b), and $\epsilon/J = 1.5$ (c); $N = 270$. Average relative deviation of the eigenstate expectation values of $\hat{N}_1$ with respect to the microcanonical average (d) and the normalized extremal fluctuations of the eigenstate expectation values of $\hat{N}_1$ (e) both as a function of the integrability breaking term ϵ. In (d) and (e), the eigenstates lie in the energy range $[E/(JN) - \Delta E/(JN), E/(JN) + \Delta E/(JN)]$ with $E/(JN) = 0.5$ and $\Delta E/(JN) = 0.1$.

To study the fluctuations of an observable around the microcanonical expectation value, we consider the devi-

ation of its eigenstate expectation value,

$$\Delta^{mic}\mathcal{O} = \frac{\sum_\alpha |\mathcal{O}_{\alpha\alpha} - \mathcal{O}_{mic}|}{\sum_\alpha \mathcal{O}_{\alpha\alpha}}, \qquad (17)$$

with respect to the microcanonical result,

$$\mathcal{O}_{mic} = \frac{1}{\mathcal{N}_{E,\Delta E}} \sum_{\substack{\alpha, \\ |E-E_\alpha|<\Delta E}} \mathcal{O}_{\alpha\alpha}, \qquad (18)$$

where $\mathcal{N}_{E,\Delta E}$ is the number of energy eigenstates with energy in the window ΔE. We also study the normalized extremal fluctuation [105],

$$\Delta_e^{mic}\mathcal{O} = |\frac{\max\mathcal{O} - \min\mathcal{O}}{\mathcal{O}_{mic}}|, \qquad (19)$$

where $\max\mathcal{O}$ and $\min\mathcal{O}$ are the maximum and minimum values of $\mathcal{O}_{\alpha\alpha}$. In Fig. 10 (d) [Fig. 10 (e)], we present the results for $\Delta^{mic}N_1$ [$\Delta_e^{mic}N_1$] for eigenstates with $E/(JN) = 0.5$ in the window of width $\Delta E/(JN) = 0.1$. The results for $(N_2)_{\alpha\alpha}$ and $(N_3)_{\alpha\alpha}$ are similar (not shown).

Figures 10 (d)-(e) are analogous to Fig. 4. They show that the smallest fluctuations of the eigenstate expectation values happen in the vicinity of $\epsilon/J \sim 1.5$, where the chaos indicator β is also the largest . The fluctuations increase as the system approaches both integrable limits, as $\epsilon/J \to 0$ (Bethe ansatz) and as $\epsilon/J \to \infty$ (self-trapping).

At a fixed value of ϵ/J, one sees that $\Delta^{mic}N_1$ in Fig. 10 (d) decreases slightly as the total number of particles increases. A discussion of how $\Delta^{mic}\mathcal{O}$ scales with the dimension D of the Hilbert for the triple-well Bose-Hubbard model is provided in Ref. [30], where it is found that the scaling does not follow expectations consistent with fully chaotic eigenstates. Similarly to our analysis of Fig. 4, the results in Fig. 10 (d) suggest that the reduction of the fluctuations for larger N's is caused by better statistics, not necessarily improved levels of chaos. Contrary to multi-well systems, our model is limited to three degrees of freedom.

Our results for the extremal fluctuations in Fig. 10 (e) add to the above discussion. We see that $\Delta_e^{mic}N_1$ does not decrease as N increases. This contrasts with the case of interacting many-body quantum systems with many sites, where the extremal fluctuations do decrease as the number of particles and wells increase. The extremal fluctuation is a more rigorous test of the validity of the ETH [105], and by extension of the degree of quantum chaos.

B. Off-diagonal elements

The strongest signatures of quantum chaos for our triple-well model happen for $\epsilon/J \sim 1.5$, but the results for level statistics [Fig. 4], structure of the eigenstates [Fig. 9], and extremal fluctuations [Fig. 10 (e)] indicate that even at this point, full chaos is not achieved. Here,

we investigate how this saturated level of chaos, in particular the non-Gaussian distribution of the eigenstates components in Fig. 9, gets reflected into the distribution of the off-diagonal elements of the number operators.

The off-diagonal elements of $\hat{N}_i$ is given by

$$
\langle \alpha | \hat{N}_i | \beta \rangle = \sum_{n=1}^{D} C_n^\alpha C_n^\beta \langle n | \hat{N}_i | n \rangle
$$
$$
= \underbrace{\sum_{n=1}^{N} C_n^\alpha C_n^\beta}_{\langle n | \hat{N}_i | n \rangle = 1} + 2 \underbrace{\sum_{n=1}^{N-1} C_n^\alpha C_n^\beta}_{\langle n | \hat{N}_i | n \rangle = 2} + \ldots + N \underbrace{\sum_{n=1}^{1} C_n^\alpha C_n^\beta}_{\langle n | \hat{N}_i | n \rangle = N}.
$$
(20)

In the case of fully chaotic eigenstates, where C_n^α's are independent Gaussian random numbers, the distribution of $(N_i)_{\alpha\beta}$ should also be Gaussian. This is evident from the equation above. The product of independent random variables is again an independent random variable, and according to the central limit theorem, the sum of random variables from any distribution follows a Gaussian distribution.

In Fig. 11, we show the distribution of the number operator of well 1 (for equivalent results for wells 2 and 3, see the appendix B 5.) As the integrability term ϵ/J increases from zero [Fig. 11 (a)] to 1.5 [Figs. 11 (c)], the peak at $(N_1)_{\alpha\beta}/N \sim 0$ decreases and the distribution gets more similar to a Gaussian, although this shape is never achieved, independently of the number of particles.
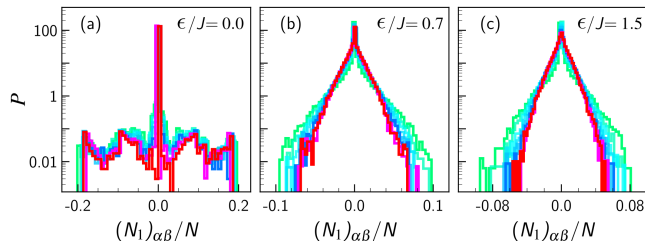
FIG. 11. Distributions of the off-diagonal elements of the number operator of well 1, $\langle \alpha | \hat{N}_1 | \beta \rangle$, for 300 eigenstates with energy $E/(JN) \sim 0.5$. The value of the integrability breaking parameter is indicated in the panels. The distributions are shown for different numbers of particles, $N = 60$ (green) to $N = 270$ (red) in increments of 30.

In Fig. 12 (a), we select only the curve for $N = 270$ from Fig. 11 (c) and show that its best fit is a Laplace distribution. Some explanations are now in order. The Laplace distribution (more precisely, a modified Bessel function of the second kind) describes the off-diagonal elements of single-particle eigenstates in chaotic quadratic Hamiltonians [108]. In this case, $N = 1$ and the only term that survives in Eq. (20) is the last one. This term is a single product of two Gaussian random variables, whose distribution is indeed Laplace. Our scenario is completely different from this one, since in Eq. (20), we have large sums of the products $C_n^\alpha C_n^\beta$.
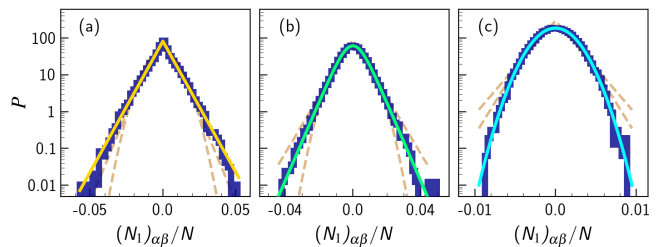
FIG. 12. Distributions of the off-diagonal elements of the number operator of well 1, $\langle \alpha | \hat{N}_1 | \beta \rangle$, for 300 eigenstates with $E/(JN) \sim 0.5$, $N = 270$, $\epsilon/J = 1.5$. The solid line indicates the best fit: (a) Laplace, (b) Logistic, and (c) Gaussian distribution. In (a), just as in Fig. 11 (c), all the components C_n^α of the eigenstates are considered. In (b), only those components for which $0.25 \leq e_n/J \leq 0.7$ are taken into account. In (c), the components are those from Gaussian random vectors.

Similar to our analysis in Fig. 9, a closer study of Fig. 12 (a) reveals that the peak at $(N_1)_{\alpha\beta}/N \sim 0$ is caused by the Fock states with energies outside the chaotic region. By removing the contributions from the states with $e_n/J < 0.25$ and $e_n/J > 0.75$, the distribution of $(N_1)_{\alpha\beta}$ becomes Logistic, as seen in Fig. 12 (b), which is closer but not yet Gaussian. If, however, we calculate Eq. (20) using eigenstates from GOE random matrices, then we finally reach the Gaussian shape, as expected from the central limit theorem and as illustrated in Fig. 12 (c).

The study of the off-diagonal elements corroborates our claims that the triple-well model in Eq. (1) do not have fully chaotic eigenstates. The same holds for the triple-well Bose-Hubbard models presented in the appendix A, where the distributions of the off-diagonal elements of the number operators are not Gaussian either.

VI. CONCLUSIONS

We investigated the spectrum, eigenstates, and occupation numbers of an integrable bosonic triple-well model that becomes chaotic with the addition of a tilting potential. The analysis of the structure of the eigenstates shows that for values of the tilt where chaos emerges, there are still regions of energy where the system remains non-chaotic. Furthermore, even within the energy interval of chaos, the eigenstates are not fully chaotic (ergodic), that is, their components do not follow Gaussian distributions and the generalized dimensions are smaller than 1, which suggest reminiscences of correlations.

Diagonal and off-diagonal ETH, that is the proximity of the infinite-time average of a local observable to the microcanonical ensemble and the Gaussian shape of the distribution of the off-diagonal elements of this observable, are also good indicators of the level of chaoticity of a many-body quantum system. None of the two are entirely fulfilled by our model. As we showed, the distributions of the off-diagonal elements of the number opera-

tors are particularly sensitive to the lack of gaussianity of the eigenstates, which prevents those distributions from becoming Gaussian.

Studies of the eigenstates and off-diagonal elements of observables can reveal details about quantum systems that are not always easily accessible from a direct study of their eigenvalues. In our specific case, the analysis of the eigenstates and observables shows that three wells constitute the preface for many-body quantum chaos.

A natural extension of our work is to examine how our results change by increasing the number of wells, the role played by the geometry of the system, and the addition of non-linear terms [109] or external drives [110, 111].

Appendix A: Bose-Hubbard Models

Bose-Hubbard models describe interacting spinless bosons on a discrete lattice [48] and are experimentally implemented with ultracold atoms in optical lattices [49]. In the case of three wells, the bare Bose-Hubbard model is represented by the Hamiltonian

$$\hat{H} = \frac{U_0}{N}\left(\hat{N}_1\left(\hat{N}_1 - 1\right) + \hat{N}_2\left(\hat{N}_2 - 1\right) + \hat{N}_3\left(\hat{N}_3 - 1\right)\right) + \frac{J}{\sqrt{2}}\left(\hat{a}_1^\dagger\hat{a}_2 + \hat{a}_2^\dagger\hat{a}_1\right) + \frac{J}{\sqrt{2}}\left(\hat{a}_2^\dagger\hat{a}_3 + \hat{a}_3^\dagger\hat{a}_2\right), \quad (A1)$$

where U_0 is the onsite interaction, J is the hopping (tunneling) parameter, and $N = N_1 + N_2 + N_3$ is the total number of particles.

This system presents signatures of quantum chaos when the number L of wells coincides with the number particles, $L = N \geq 5$ [51]. However, as shown in [30], the model is also chaotic for only 3 sites and $N \gg 3$. Notice that the Hamiltonian has parity symmetry, so to study level statistics, one should either break this symmetry, as done in [30], or separate the eigenvalues by symmetry sector. An alternative is to resort to the correlation hole, which detects level repulsion even in the presence of symmetries [82, 89].

The extended version of the Bose-Hubbard model,

$$\hat{H} = \frac{U_0}{N}\left(\hat{N}_1\left(\hat{N}_1 - 1\right) + \hat{N}_2\left(\hat{N}_2 - 1\right) + \hat{N}_3\left(\hat{N}_3 - 1\right)\right) + \frac{U_1}{N}\left(\hat{N}_1\hat{N}_2 + \hat{N}_2\hat{N}_3 + \frac{1}{\alpha}(\hat{N}_1\hat{N}_3)\right) + \frac{J}{\sqrt{2}}\left(\hat{a}_1^\dagger\hat{a}_2 + \hat{a}_2^\dagger\hat{a}_1\right) + \frac{J}{\sqrt{2}}\left(\hat{a}_2^\dagger\hat{a}_3 + \hat{a}_3^\dagger\hat{a}_2\right), \quad (A2)$$

includes also interactions between the wells, which emerge in dipolar gases. As discussed in [37], the parameter α depends on the geometry of the trap and can vary between $4 \leq \alpha \leq 8$. The extended Bose-Hubbard model also has parity symmetry through exchange of wells 1 and 3. Depending on the choices of parameters and with some rearrangement of the signs, Eq. (A2) coincides with the Hamiltonian of our model in Eq. (1) in the integrable limit.

In Fig. 13, we show the DOS for the two Bose-Hubbard models above for parameters that lead to approximate Wigner-Dyson distributions. For $N = 180$ and the positive parity sector, we get Brody factors $\beta \approx 0.8$. Figure 13 can be compared with the DOS for the chaotic triple-well model with the external tilt in Fig. 3 (c). None of the distributions, that in Fig. 3 (c) or the ones in Fig. 13, have a Gaussian shape.
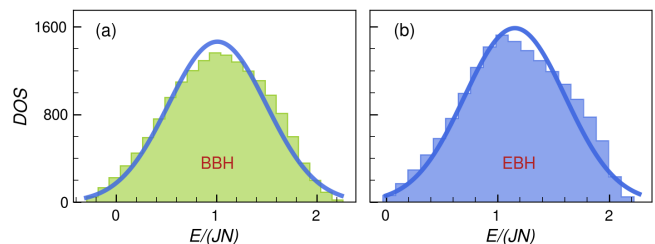

FIG. 13. Density of states for (a) the bare Bose-Hubbard model from Eq. (A1) and (b) the extended Bose-Hubbard model from Eq. (A2). All eigenvalues from both symmetry sectors are considered; $N = 180$. The parameters used lead to Wigner-Dyson distributions: (a) $U_0/J = 2.03$, (b) $U_0/J = 1.85$, $U_1/J = 1.2$ and $\alpha = 2\sqrt{2}$. The solid lines are Gaussian fits.

In Fig. 14, we show results for the Shannon entropy, components of the eigenstates, and off-diagonal elements of $\hat{N}_1$ for both Bose-Hubbard models in the chaotic domain. The plot for the Shannon entropy in Fig. 14 (a), and Fig. 14 (d) can be compared with Fig. 6. Similarly to our model, the Bose-Hubbard models present a region of energy away from the edges of the spectrum where the entropy is larger and has smaller fluctuations. As we move closer to borders of the spectrum, a pattern of regular lines similar to those in Fig. 6 appear.

We studied the distributions of the components of various eigenstates in the chaotic region of the spectrum, with energy $E/(JN) \sim 1$ [$E/(JN) \sim 1.4$] for the bare Bose-Hubbard model [extended Bose-Hubbard model]. In most cases, the best fit is a Logistic distribution, as

illustrated in Fig. 14 (b) [Fig. 14 (e)]. For the Bose-Hubbard models, we do not find an excessive number of $C_n^\alpha \sim 0$ as in Fig. 9 (a), but the tails are still longer than in Gaussian distributions.

The lack of gaussianity of the eigenstates result in the non-Gaussian distributions of the off-diagonal elements of the number operators. This is illustrated in Fig. 14 (c) and Fig. 14 (f) for $\hat{N}_1$. Contrary to Fig. 12, none of the usual distributions, Laplace, Logistic, Gaussian, or Lorentzian, capture well the histogram for $(N_1)_{\alpha\beta}$.
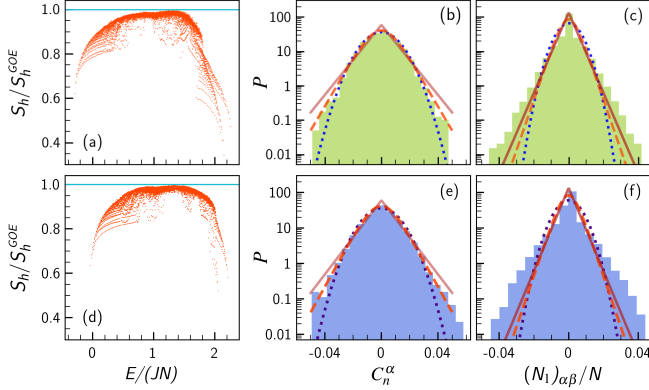

FIG. 14. Shannon entropy (a,d), distribution of the components of an eigenstate in the chaotic region (b,e), and distribution of the off-diagonal elements of the number operator of well 1 (c,f) for the bare Bose-Hubbard model (a)-(c) and the extended Bose-Hubbard model (d)-(f) in the positive parity sector; $N = 180$. The parameters are the same as in Fig. 13. In (a,d): Solid line indicates the result for random matrix theory. In (b,c,e,f): Solid line represents the Laplace; dashed line, the Logistic; and dotted line, the Gaussian distribution. The best fit in (b) and (e) is the Logistic distribution. In (b), $E/(JN) = 1.16$ and in (e), $E/(JN) = 1.33$.

Appendix B: Additional results for our triple-well model

We leave to this appendix some further details about our triple-well model. This includes the dependence of the timescales of the spectral form factor on N, a plot for the participation ratio, and the distributions of off-diagonal elements for the number operators of the three wells.

1. Timescales for the spectral form factor

The time $t_{\min}$ to reach the minimum of the correlation hole and the time for the saturation of the spectral form factor (Heisenberg time) can be derived using the analytical expression in Eq. (7).

a. Time for the minimum of the correlation hole

To determine the time $t_{\min}$, we consider the envelope of the initial oscillatory decay, $\sin^2(\sigma t) \to 1$, (the choice $\sin^2(\sigma t) \to 1/2$ would also be suitable) and use the expression of the function $b_2(t/(2\pi\nu_c))$ for short times, $t \leq 2\pi\nu_c$. The latter is justified, because the minimum of $S_{FF}(t)$ is the point where the function $[\eta \sin^2(\sigma t)]/(\sigma t)^2$, that causes the decay of the spectral form factor, meets the $b_2(t/(2\pi\nu_c))$ function, which is responsible for bringing $S_{FF}(t)$ up to saturation. The time is then obtained from

$$\frac{dS_{FF}^{analyt}}{dt} = 0 \tag{B1}$$

$$\frac{4\eta}{\sigma^2 t_{\min}^3} = \frac{1}{\pi\nu_c} + \frac{1}{\pi\nu_c(1 + \frac{t_{\min}}{\pi\nu_c})} - \frac{\ln\left(1 + \frac{t_{\min}}{\pi\nu_c}\right)}{\pi\nu_c},$$

which can be solved numerically to determine $t_{\min}$. By expanding the equation above, using $t_{\min} \ll \pi\nu_c$, we get that

$$t_{\min} = \left(\frac{2\pi\nu_c\eta}{\sigma^2}\right)^{1/3} = \left(\frac{16\pi}{9\langle\overline{S_{FF}}\rangle^2\sigma^3}\right)^{1/3}. \tag{B2}$$

Since $\langle\overline{S_{FF}}\rangle$ scales with the inverse of the dimension of the Hilbert space, that is $\langle\overline{S_{FF}}\rangle \propto N^{-2}$, and $\sigma \propto N$, we have that $t_{\min}$ grows with the number of particles as

$$t_{\min} \propto N^{1/3}. \tag{B3}$$

This is confirmed numerically for all N's considered here, as indicated by the values of $t_{\min}$ marked with circles in Fig. 5.

b. Saturation time

The saturation time, t_S, corresponds to the time when $S_{FF}(t)$ reaches its infinite-time average $\langle\overline{S_{FF}}\rangle$. At these very long times, only the b_2 function is relevant, and since it shows a power-law behavior, $b_2\left(\frac{t}{2\pi\nu_c}\right) \to \frac{\pi^2\nu_c^2}{3t^2}$, the complete saturation is not well determined [95]. We define t_S as the moment when $S_{FF}(t_S) = (1 - \delta)\langle\overline{S_{FF}}\rangle$, where δ is a small value that guarantees that $S_{FF}(t)$ is already within the fluctuations around the infinite-time average. This gives

$$\frac{t_S}{2\pi\nu_c}\ln\left(\frac{t_S/\pi\nu_c + 1}{t_S/\pi\nu_c - 1}\right) = \delta\frac{(\eta - 1)\langle\overline{S_{FF}}\rangle}{1 - \langle\overline{S_{FF}}\rangle} + 1 \tag{B4}$$

and using that $t_S \gg \pi\nu_c$, we arrive at

$$t_S = \frac{\pi\nu_c}{2\sqrt{\delta}} \propto N, \tag{B5}$$

which shows that the saturation time grows linearly with N, as confirmed in Fig. 5, where t_S is marked with diamonds.

It is instructive to compare $t_{\min}$ and t_S for our model with the same timescales for the Dicke model [93], which has two degrees of freedom, and for the one-dimensional disordered spin-1/2 model with many excitations [95], which has many degrees of freedom and a Hilbert space that grows exponentially with the number of sites. While for our model and the Dicke model, $t_{\min}$ scales with the number of particles as $N^{1/3}$ and $N^{1/2}$, respectively, and $t_S \propto N$, for the interacting many-body spin system, $t_{\min}$ grows with the size of the Hilbert space as $D^{2/3}$ and $t_R \propto D$. Based on these timescales, it might be possible to detect the correlation hole experimentally with the triple-well model, but more unlikely to get this done with many-body systems with many sites and short-range couplings.

2. Participation ratio in the Fock basis

We show in Fig. 15 the participation ratio obtained for eigenstates written in the Fock basis and divided by the result for GOE random matrices, $P_R^{GOE} \sim D/3$. In comparison to the results for the Shannon entropy presented in Fig. 6, we see that the fluctuations are larger for the participation ratio.
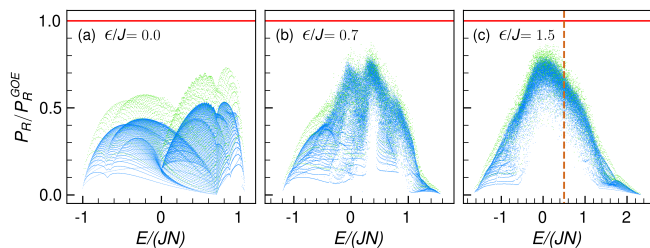

FIG. 15. Participation ratio as a function of energy for $N = 90$ (light green dots) and $N = 270$ (blue dots). The solid horizontal lines mark the results for GOE random matrices. The dashed vertical line in (c) marks approximately the center of the chaotic region.

The fluctuations decrease as the system moves from the integrable limit of Fig. 15 (a) to the chaotic domain of Fig. 15 (c), but even for $\epsilon = 1.5$, we still find regions closer to the edges of the spectrum with patterns of lines similar to those found in the regular regime. In addition, the participation ratio is throughout smaller than P_R^{GOE} and this does not improve as N increases [cf. $N = 270$ (dark dots) with $N = 90$ (light dots)].

3. Shannon entropy in the zero-detuning basis

When computing delocalization measures, the results depend on the basis used. The basis choice is done according to the question under investigation. Our studies of ETH focus on the occupations of each well, which are observables measured in cold atoms. It is therefore natural to perform the analysis of the eigenstates in a basis,

where $\hat{N}_i$ is diagonal, that is, in the Fock basis $|n\rangle$, as done in Sec. IV. In studies of the transition to chaos, however, the most appropriate basis corresponds to the eigenstates of the integrable part of the model considered. In our case, this basis coincides with the eigenstates $|\phi\rangle$ of the Hamiltonian in Eq. (1) with zero detuning ($\epsilon = 0$).

The purpose of Fig. 16 is to compare the Shannon entropy calculated in the Fock basis $|n\rangle$ in Fig. 6 (b) and Fig. 6 (c) [light points in Fig. 16 (a) and Fig. 16 (b)] with the Shannon entropy computed in the zero-detuning basis $|\phi\rangle$ [dark points in Fig. 16 (a) and Fig. 16 (b)]. The data show that using this zero-detuning basis does not qualitatively change the results for $\epsilon/J = 0.7$ and $\epsilon/J = 1.5$. For $\epsilon/J = 0.7$ in Fig. 16 (a), patches of high degrees of delocalization appear for both bases for $E/(JN) \sim 0.3$ and $E/(JN) \sim 0.9$; and for $\epsilon/J = 1.5$ in Fig. 16 (b), the chaotic region is evident for both bases for $E/(JN) \in [-0.2, 1]$.
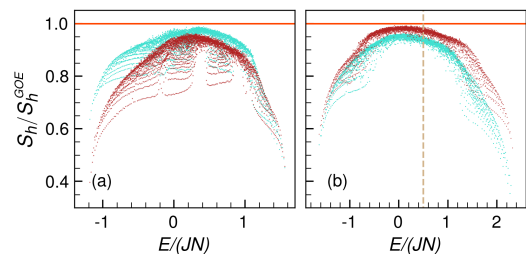

FIG. 16. Shannon entropy S_h in the Fock basis (light dots, as in Fig. 6) and in the zero-detuning basis (dark dots) as a function of energy for $N = 90$, $U/J = 0.7$, and $\epsilon/J = 0.7$ (a) [$\epsilon/J = 1.5$ (b)]. The solid horizontal lines mark the results for GOE full random matrices. The dashed vertical line in (b) marks approximately the center of the chaotic region.

If we compare the value of S_h/S_h^{GOE} as a function of ϵ/J, from $\epsilon = 0$ to $\epsilon/J = 1.5$, it grows dramatically for the zero-detuning basis, since in this case, $S_h^{|\phi\rangle}(\epsilon = 0) = 0$. One also notices that $S_h^{(|\phi\rangle)}(\epsilon = 1.5)/S_h^{GOE}$ reaches values closer to 1 for the zero-detunig basis than $S_h^{(|n\rangle)}(\epsilon = 1.5)/S_h^{GOE}$ for the Fock basis. But the overall structure of the eigenstates for ϵ/J in the chaotic region does not change much from one basis to the other, as suggested by Fig. 16 and by the results below in Fig. 17.

4. Distribution of the components of the eigenstates in the zero-detuning basis

The distributions of all the components of an eigenstate written in the zero-detuning basis and having energy close to the middle of the chaotic region is given in Fig. 17 (a). In contrast with the case of the Fock basis presented in Fig. 9 (a), here we did not find an excessive number of zero valued components. Yet, in Fig. 17 (b), we follow the same procedure used in Fig. 9 (b) and kept only the components associated with states that have

energy in $[-0.2, 1]$. With that, the small central peak in Fig. 17 (a) is erased.

Similarly to what is observed in Fig. 9 (b), the best fit in Fig. 17 (b) [and even in Fig. 17 (a)] is again Logistic instead of Gaussian. This indicates that the eigenstates of our triple-well model written in the zero-detuning basis, just as in the Fock basis, are not ergodic.
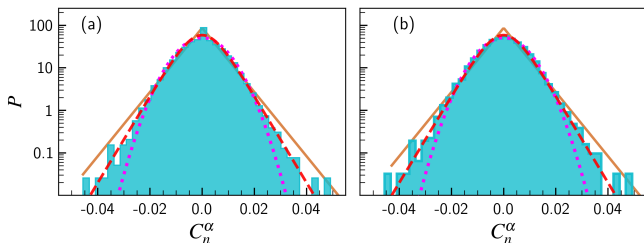
5. Distributions of off-diagonal elements

In the main text, we show the distribution of the off-diagonal elements of the number operators of well 1 in Fig. 12 (a). Here, we repeat this figure in Fig. 18 (a), but show also the distributions of the off-diagonal elements of the number operators of well 2 (b) and 3 (c) in comparison with Laplace, Logistic, and Gaussian distributions. The best fit for the three observables is the Laplace distribution.
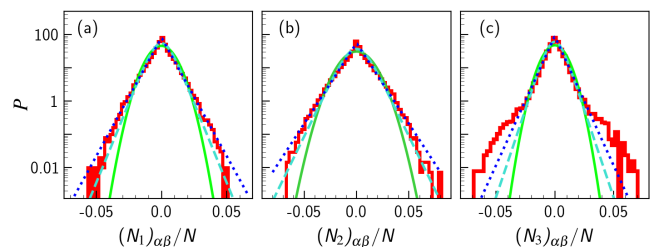

FIG. 17. Distributions of the components C_n^α of an eigenstate with energy $E/(JN) \sim 0.5$; $N = 180$, $U/J = 0.7$ and $\epsilon/J = 1.5$. In (a), all components are considered, while in (b), only those for states with energy in $[-0.2, 1]$ are kept. Solid line: Laplace distribution; dashed line: Logistic distribution; dotted line: Gaussian distribution.

FIG. 18. Distributions of the off-diagonal elements of (a) $\hat{N}_1$, (b) $\hat{N}_2$, and (c) $\hat{N}_3$ for 300 eigenstates with energy $E/(JN) \sim 0.5$; $N = 270$, $U/J = 0.7$ and $\epsilon/J = 1.5$. The fitting curves correspond to Laplace (dashed line), Logistic (dashed line) and Gaussian (solid line) distributions.

[1] V. Zelevinsky, B. Brown, N. Frazier, and M. Horoi, The nuclear shell model as a testing ground for many-body quantum chaos, Phys. Rep. **276**, 85 (1996).

[2] F. Borgonovi, F. M. Izrailev, L. F. Santos, and V. G. Zelevinsky, Quantum chaos and thermalization in isolated systems of interacting particles, Phys. Rep. **626**, 1 (2016).

[3] L. D. Alessio, Y. Kafri, A. Polkovnikov, and M. Rigol, From quantum chaos and eigenstate thermalization to statistical mechanics and thermodynamics, Adv. Phys. **65**, 239 (2016).

[4] J. Maldacena, S. H. Shenker, and D. Stanford, A bound on chaos, J. High Energy Phys. **2016** (8), 106.

[5] Z. Zhang, V. Dunjko, and M. Olshanii, Atom transistor from the point of view of nonequilibrium dynamics, New J. Phys. **17**, 125008 (2015).

[6] S. C. Caliga, C. J. E. Straatsma, and D. Z. Anderson, Transport dynamics of ultracold atoms in a triple-well transistor-like potential, N. J. Phys. **18**, 025010 (2016).

[7] O. Marchukov, A. Volosniev, M. Valiente, D. Petrosyan, and N. Zinner, Quantum spin transistor with a Heisenberg spin chain, Nat. Commun. **7**, 1 (2016).

[8] T. F. Viscondi, K. Furuya, and M. C. de Oliveira, Phase transition, entanglement and squeezing in a triple-well condensate, EPL (Europhys. Lett.) **90**, 10014 (2010).

[9] A. P. Tonel, L. H. Ymai, K. W. Wilsmann, A. Foerster, and J. Links, Entangled states of dipolar bosons generated in a triple-well potential, SciPost Phys. Core **2**, 3 (2020).

[10] C. J. Bradly, M. Rab, A. D. Greentree, and A. M. Martin, Coherent tunneling via adiabatic passage in a three-well Bose-Hubbard system, Phys. Rev. A **85**, 053609 (2012).

[11] B. Xiong and U. R. Fischer, Interaction-induced coherence among polar bosons stored in triple-well potentials, Phys. Rev. A **88**, 063608 (2013).

[12] Z. Zhou, W. Hai, Q. Xie, and J. Tan, Second-order tunneling of two interacting bosons in a driven triple well, New J. Phys. **15**, 123020 (2013).

[13] M. K. Olsen, Quantum dynamics and entanglement in coherent transport of atomic population, J. Phys. B **47**, 095301 (2014).

[14] A. Gallemí, M. Guilleumas, R. Mayol, and A. Sanpera, Role of anisotropy in dipolar bosons in triple-well potentials, Phys. Rev. A **88**, 063645 (2013).

[15] A. Gallemí, M. Guilleumas, J. Martorell, R. Mayol, A. Polls, and B. Juliá-Díaz, Fragmented condensation in Bose–Hubbard trimers with tunable tunnelling, New J. Phys. **17**, 073014 (2015).

[16] K. Nemoto, C. A. Holmes, G. J. Milburn, and W. J. Munro, Quantum dynamics of three coupled atomic Bose-Einstein condensates, Phys. Rev. A **63**, 013604 (2000).

[17] R. Franzosi and V. Penna, Self-trapping mechanisms in the dynamics of three coupled Bose-Einstein condensates, Phys. Rev. A **65**, 013601 (2001).

[18] E. M. Graefe, H. J. Korsch, and D. Witthaut, Mean-field dynamics of a Bose-Einstein condensate in a time-dependent triple-well trap: Nonlinear eigenstates, Landau-Zener models, and stimulated Raman adiabatic passage, Phys. Rev. A **73**, 013617 (2006).

[19] M. Hiller, T. Kottos, and T. Geisel, Complexity in parametric Bose-Hubbard Hamiltonians and structural analysis of eigenstates, Phys. Rev. A **73**, 061604 (2006).

[20] B. Liu, L.-B. Fu, S.-P. Yang, and J. Liu, Josephson oscillation and transition to self-trapping for Bose-Einstein condensates in a triple-well trap, Phys. Rev. A **75**, 033601 (2007).

[21] M. Hiller, T. Kottos, and T. Geisel, Wave-packet dynamics in energy space of a chaotic trimeric Bose-Hubbard system, Phys. Rev. A **79**, 023621 (2009).

[22] E. R. Castro, J. Chávez-Carlos, I. Roditi, L. F. Santos, and J. G. Hirsch, Quantum-classical correspondence of a system of interacting bosons in a triple-well potential, Quantum **5**, 563 (2021).

[23] S. Flach and V. Fleurov, Tunnelling in the nonintegrable trimer - a step towards quantum breathers, J. Phys. Condensed Matter **9**, 7039 (1997).

[24] M. A. Garcia-March, S. van Frank, M. Bonneau, J. Schmiedmayer, M. Lewenstein, and L. F. Santos, Relaxation, chaos, and thermalization in a three-mode model of a Bose–Einstein condensate, New J. Phys. **20**, 113039 (2018).

[25] A. Richaud and V. Penna, Phase separation can be stronger than chaos, New J. Phys. **20**, 105008 (2018).

[26] S. Bera, R. Roy, A. Gammal, B. Chakrabarti, and B. Chatterjee, Probing relaxation dynamics of a few strongly correlated bosons in a 1D triple well optical lattice, J. Phys. B **52**, 215303 (2019).

[27] R. Bürkle, A. Vardi, D. Cohen, and J. R. Anglin, Probabilistic Hysteresis in Integrable and Chaotic Isolated Hamiltonian Systems, Phys. Rev. Lett. **123**, 114101 (2019).

[28] S. Ray, D. Cohen, and A. Vardi, Chaos-induced breakdown of Bose-Hubbard modeling, Phys. Rev. A **101**, 013624 (2020).

[29] M. Rautenberg and M. Gärttner, Classical and quantum chaos in a three-mode bosonic system, Phys. Rev. A **101**, 053604 (2020).

[30] G. Nakerst and M. Haque, Eigenstate thermalization scaling in approaching the classical limit, Phys. Rev. E **103**, 042109 (2021).

[31] G. Arwas, A. Vardi, and D. Cohen, Triangular Bose-Hubbard trimer as a minimal model for a superfluid circuit, Phys. Rev. A **89**, 013601 (2014).

[32] G. Arwas, A. Vardi, and D. Cohen, Superfluidity and Chaos in low dimensional circuits, Sci. Rep. **5**, 13433 (2015).

[33] C. Khripkov, A. Vardi, and D. Cohen, Many-body dynamical localization and thermalization, Phys. Rev. A **101**, 043603 (2020).

[34] W. Kirkby, Y. Yee, K. Shi, and D. H. J. O'Dell, Caustics in quantum many-body dynamics, Phys. Rev. Research **4**, 013105 (2022).

[35] A. Foerster and E. Ragoucy, Exactly solvable models in atomic and molecular physics, Nuclear Physics B **777**, 373 (2007).

[36] P. Buonsante, R. Franzosi, and V. Penna, Control of unstable macroscopic oscillations in the dynamics of three coupled Bose condensates, J. Phys. A **42**, 285307 (2009).

[37] T. Lahaye, T. Pfau, and L. Santos, Mesoscopic Ensembles of Polar Bosons in Triple-Well Potentials, Phys. Rev. Lett. **104**, 170404 (2010).

[38] A. I. Streltsov, K. Sakmann, O. E. Alon, and L. S. Cederbaum, Accurate multi-boson long-time dynamics

[39] in triple-well periodic traps, Phys. Rev. A **83**, 043604 (2011).

[39] T. F. Viscondi and K. Furuya, Dynamics of a Bose–Einstein condensate in a symmetric triple-well trap, J. Phys. A **44**, 175301 (2011).

[40] L. Cao, I. Brouzos, S. Zöllner, and P. Schmelcher, Interaction-driven interband tunneling of bosons in the triple well, New J. Phys. **13**, 033032 (2011).

[41] I. Tikhonenkov, A. Vardi, J. R. Anglin, and D. Cohen, Minimal Fokker-Planck Theory for the Thermalization of Mesoscopic Subsystems, Phys. Rev. Lett. **110**, 050401 (2013).

[42] Q. Guo, X. Chen, and B. Wu, Tunneling dynamics and band structures of three weakly coupled Bose-Einstein condensates, Opt. Express **22**, 19219 (2014).

[43] G. M. Koutentakis, S. I. Mistakidis, and P. Schmelcher, Quench-induced resonant tunneling mechanisms of bosons in an optical lattice with harmonic confinement, Phys. Rev. A **95**, 013617 (2017).

[44] A. Dey, D. Cohen, and A. Vardi, Adiabatic Passage through chaos, Phys. Rev. Lett. **121**, 250405 (2018).

[45] L. Guo, L. Du, C. Yin, Y. Zhang, and S. Chen, Dynamical evolutions in non-hermitian triple-well systems with a complex potential, Phys. Rev. A **97**, 032109 (2018).

[46] S. Dutta, M. C. Tsatsos, S. Basu, and A. U. J. Lode, Management of the correlations of UltracoldBosons in triple wells, New J. Phys. **21**, 053044 (2019).

[47] G. McCormack, R. Nath, and W. Li, Nonlinear dynamics of Rydberg-dressed Bose-Einstein condensates in a triple-well potential, Phys. Rev. A **102**, 063329 (2020).

[48] M. P. A. Fisher, P. B. Weichman, G. Grinstein, and D. S. Fisher, Boson localization and the superfluid-insulator transition, Phys. Rev. B **40**, 546 (1989).

[49] I. Bloch, Ultracold quantum gases in optical lattices, Nat. Phys. **1**, 23 (2005).

[50] T. Choy and F. Haldane, Failure of Bethe–Ansatz solutions of generalisations of the Hubbard chain to arbitrary permutation symmetry, Phys. Lett. A **90**, 83 (1982).

[51] A. R. Kolovsky and A. Buchleitner, Quantum chaos in the Bose-Hubbard model, Europhysics Letters (EPL) **68**, 632 (2004).

[52] N. Oelkers and J. Links, Ground-state properties of the attractive one-dimensional Bose-Hubbard model, Phys. Rev. B **75**, 115119 (2007).

[53] C. Kollath, G. Roux, G. Biroli, and A. M. Läuchli, Statistical properties of the spectrum of the extended Bose-Hubbard model, J. Stat. Mech. Theory Exp. **2010**, P08011 (2010).

[54] L. H. Ymai, A. P. Tonel, A. Foerster, and J. Links, Quantum integrable multi-well tunneling models, J. Phys. A **50**, 264001 (2017).

[55] K. W. Wilsmann, L. H. Ymai, A. P. Tonel, J. Links, and A. Foerster, Control of tunneling in an atomtronic switching device, Comm. Phys. **1** (2018).

[56] With four wells, this model has also been used in interferometry [112], and for NOON states generation [113].

[57] A. J. Leggett, Bose-Einstein condensation in the alkali gases: Some fundamental concepts, Rev. Mod. Phys. **73**, 307 (2001).

[58] A. P. Tonel, J. Links, and A. Foerster, Quantum dynamics of a model for two Josephson-coupled Bose–Einstein condensates, J. Phys. A **38**, 1235 (2005).

[59] J. Links, A. Foerster, A. Tonel, and G. Santos, The two-site Bose-Hubbard model, Ann. Henri Poincaré **7**, 1591 (2006).

[60] L. Dell'Anna, G. Mazzarella, V. Penna, and L. Salasnich, Entanglement entropy and macroscopic quantum states with dipolar bosons in a triple-well potential, Phys. Rev. A **87**, 053620 (2013).

[61] I. Ferrier-Barbut, H. Kadau, M. Schmitt, M. Wenzel, and T. Pfau, Observation of quantum droplets in a strongly dipolar ose gas, Phys. Rev. Lett. **116**, 215301 (2016).

[62] L. Chomaz, D. Petter, P. Ilzhöfer, G. Natale, A. Trautmann, C. Politi, G. Durastante, R. M. W. van Bijnen, A. Patscheider, M. Sohmen, M. J. Mark, and F. Ferlaino, Long-lived and transient supersolid behaviors in dipolar quantum gases, Phys. Rev. X **9**, 021012 (2019).

[63] Forthcoming publication.

[64] A. P. Tonel, J. Links, and A. Foerster, Behaviour of the energy gap in a model of Josephson coupled Bose–Einstein condensates, J. Phys. A **38**, 6879 (2005).

[65] F. Haake, *Quantum Signatures of Chaos* (Springer-Verlag, Berlin, 1991).

[66] T. Guhr, A. Mueller-Gröeling, and H. A. Weidenmüller, Random Matrix Theories in Quantum Physics: Common Concepts, Phys. Rep. **299**, 189 (1998).

[67] M. V. Berry and M. Tabor, Level clustering in the regular spectrum, Proc. R. Soc. Lond. A **356**, 375 (1977).

[68] A. Pandey and R. Ramaswamy, Level spacings for harmonic-oscillator systems, Phys. Rev. A **43**, 4237 (1991).

[69] B. V. Chirikov and D. L. Shepelyansky, Shnirelman Peak in Level Spacing Statistics, Phys. Rev. Lett. **74**, 518 (1995).

[70] L. F. Santos, F. Borgonovi, and F. M. Izrailev, Onset of chaos and relaxation in isolated systems of interacting spins: Energy shell approach, Phys. Rev. E **85**, 036209 (2012).

[71] L. Pausch, E. G. Carnio, A. Buchleitner, and A. Rodríguez, Chaos in the Bose-Hubbard model and random two-body Hamiltonians (2021), arXiv:2109.06236.

[72] J. French and S. Wong, Validity of random matrix theories for many-particle systems, Phys. Lett. B **33**, 449 (1970).

[73] T. A. Brody, J. Flores, J. B. French, P. A. Mello, A. Pandey, and S. S. M. Wong, Random-matrix physics: spectrum and strength fluctuations, Rev. Mod. Phys. **53**, 385 (1981).

[74] M. A. Bastarrachea-Magnani, S. Lerma-Hernández, and J. G. Hirsch, Comparative quantum and semiclassical analysis of atom-field systems. I. Density of states and excited-state quantum phase transitions, Phys. Rev. A **89**, 032101 (2014).

[75] M. Schiulaz, M. Távora, and L. F. Santos, From few- to many-body quantum systems, Quantum Sci. Technol. **3**, 044006 (2018).

[76] T. Fogarty, M. Á. García-March, L. F. Santos, and N. L. Harshman, Probing the edge between integrability and quantum chaos in interacting few-atom systems, Quantum **5**, 486 (2021).

[77] M. L. Mehta, *Random Matrices* (Elsevier Academic Press, Amsterdam, 2004).

[78] As mentioned above, this excludes integrable models with picket-fence kind of spectra [67–69] and also integrable models with an excessive number of degeneracies [114].

[79] F. M. Izrailev, Simple models of quantum chaos: Spectrum and eigenfunctions, Phys. Rep. **196**, 299 (1990).

[80] L. F. Santos and M. Rigol, Onset of quantum chaos in one-dimensional bosonic and fermionic systems and its relation to thermalization, Phys. Rev. E **81**, 036206 (2010).

[81] M. Rigol and L. F. Santos, Quantum chaos and thermalization in gapped systems, Phys. Rev. A **82**, 011604(R) (2010).

[82] L. F. Santos, F. Pérez-Bernal, and E. J. Torres-Herrera, Speck of chaos, Phys. Rev. Research **2**, 043034 (2020).

[83] L. Leviandier, M. Lombardi, R. Jost, and J. P. Pique, Fourier Transform: A Tool to Measure Statistical Level Properties in Very Complex Spectra, Phys. Rev. Lett. **56**, 2449 (1986).

[84] T. Guhr and H. Weidenmüller, Correlations in anticrossing spectra and scattering theory. Analytical aspects, Chem. Phys. **146**, 21 (1990).

[85] J. Wilkie and P. Brumer, Time-dependent manifestations of quantum chaos, Phys. Rev. Lett. **67**, 1185 (1991).

[86] Y. Alhassid and R. D. Levine, Spectral autocorrelation function in the statistical theory of energy levels, Phys. Rev. A **46**, 4650 (1992).

[87] T. Gorin and T. H. Seligman, Signatures of the correlation hole in total and partial cross sections, Phys. Rev. E **65**, 026214 (2002).

[88] E. J. Torres-Herrera and L. F. Santos, Dynamical manifestations of quantum chaos: correlation hole and bulge, Philos. Trans. Royal Soc. A **375**, 20160434 (2017).

[89] J. de la Cruz, S. Lerma-Hernández, and J. G. Hirsch, Quantum chaos in a system with high degree of symmetries, Phys. Rev. E **102**, 032208 (2020).

[90] R. E. Prange, The spectral form factor is not self-averaging, Phys. Rev. Lett. **78**, 2280 (1997).

[91] M. Schiulaz, E. J. Torres-Herrera, F. Pérez-Bernal, and L. F. Santos, Self-averaging in many-body quantum systems out of equilibrium: Chaotic systems, Phys. Rev. B **101**, 174312 (2020).

[92] M. Winer and B. Swingle, Hydrodynamic theory of the connected spectral form factor (2021), arXiv:2012.01436.

[93] S. Lerma-Hernández, D. Villaseñor, M. A. Bastarrachea-Magnani, E. J. Torres-Herrera, L. F. Santos, and J. G. Hirsch, Dynamical signatures of quantum chaos and relaxation time scales in a spin-boson system, Phys. Rev. E **100**, 012218 (2019).

[94] E. J. Torres-Herrera, A. M. García-García, and L. F. Santos, Generic dynamical features of quenched interacting quantum systems: Survival probability, Density imbalance, and out-of-time-ordered correlator, Phys. Rev. B **97**, 060303 (2018).

[95] M. Schiulaz, E. J. Torres-Herrera, and L. F. Santos, Thouless and relaxation time scales in many-body quantum systems, Phys. Rev. B **99**, 174313 (2019).

[96] L. A. Khalfin, Contribution to the decay theory of a quasi-stationary state, Sov. Phys. JETP **6**, 1053 (1958).

[97] M. Távora, E. J. Torres-Herrera, and L. F. Santos, Inevitable power-law behavior of isolated many-body quantum systems and how it anticipates thermalization,

Phys. Rev. A **94**, 041603 (2016).

[98] Y. Yang, S. Iblisdir, J. I. Cirac, and M. C. Bañuls, Probing thermalization through spectral analysis with matrix product operators, Phys. Rev. Lett. **124**, 100602 (2020).

[99] E. J. Torres-Herrera, J. Karp, M. Távora, and L. F. Santos, Realistic Many-Body Quantum Systems vs. Full Random Matrices: Static and Dynamical Properties, Entropy **18**, 359 (2016).

[100] Forthcoming publication.

[101] J. W. Tukey, Exploratory data analysis., 1977, Massachusetts: Addison-Wesley (1976).

[102] A. Solórzano, L. F. Santos, and E. J. Torres-Herrera, Multifractality and self-averaging at the many-body localization transition, Phys. Rev. Research **3**, L032030 (2021).

[103] F. Wegner, Inverse participation ratio in $2 + \varepsilon$ dimensions, Z. Phys. B **36**, 209 (1980).

[104] F. Evers and A. D. Mirlin, Anderson transitions, Rev. Mod. Phys. **80**, 1355 (2008).

[105] L. F. Santos and M. Rigol, Localization and the effects of symmetries in the thermalization properties of one-dimensional quantum systems, Phys. Rev. E **82**, 031130 (2010).

[106] W. Beugeling, R. Moessner, and M. Haque, Off-diagonal matrix elements of local operators in many-body quantum systems, Phys. Rev. E **91**, 012144 (2015).

[107] In interacting many-body quantum systems, deviations from Gaussian distributions occur for many-body ob-

servables [115]. If the Hamiltonian is quadratic, deviations happen also for few-body observables [108].

[108] P. Łydżba, Y. Zhang, M. Rigol, and L. Vidmar, Single-particle eigenstate thermalization in quantum-chaotic quadratic Hamiltonians (2021), arXiv:2109.06895.

[109] D. Rubeni, J. Links, P. S. Isaac, and A. Foerster, Two-site Bose-Hubbard model with nonlinear tunneling: Classical and quantum analysis, Phys. Rev. A **95**, 043607 (2017).

[110] R. A. Kidd, M. K. Olsen, and J. F. Corney, Quantum chaos in a Bose-Hubbard dimer with modulated tunneling, Phys. Rev. A **100**, 013625 (2019).

[111] R. A. Kidd, A. Safavi-Naini, and J. F. Corney, Thermalization in a Bose-Hubbard dimer with modulated tunneling, Phys. Rev. A **102**, 023330 (2020).

[112] D. Grun, L. Ymai, K. W. Wittmann, A. Tonel, A. Foerster, and J. Links, Integrable atomtronic interferometry (2020), arXiv:2004.11987.

[113] D. Grun, K. W. Wittmann, L. Ymai, J. Links, and A. Foerster, Protocol designs for NOON states, Comm. Phys. **5**, 36 (2022).

[114] P. R. Zangara, A. D. Dente, E. J. Torres-Herrera, H. M. Pastawski, A. Iucci, and L. F. Santos, Time fluctuations in isolated quantum systems of interacting particles, Phys. Rev. E **88**, 032913 (2013).

[115] I. M. Khaymovich, M. Haque, and P. A. McClarty, Eigenstate Thermalization, Random Matrix Theory, and Behemoths, Phys. Rev. Lett. **122**, 070601 (2019).